S.T. Yau High School Science Award

Research Report

The Team

Name of team member:Junru Niu
School:Abington Friends School
City, Country:Jenkintown, America

Name of supervising teacher:Lin Wang
Job Title:Ph.D
School/Institution:East China Normal University
City, Country:Shanghai, China

Title of Research Report

Multimodal Perception in a Single Self-Bent HfS2 for Artificial Synapses and Nociceptors

Date

August 24th

Multimodal Perception in a Single Self-Bent HfS2 for Artificial Synapses and Nociceptors

Junru Niu

Abstract

Leveraging the spontaneous bending behavior of two-dimensional HfS_2, we present a flexible device capable of optoelectronic synergistic perception for emulating biological synapses and nociceptors. Structural and electronic characterizations via Raman spectroscopy, atomic force microscopy, and Kelvin probe force microscopy reveal that bending induces strain-driven type-II intramolecular heterojunctions in HfS_2, enhancing carrier separation. Optical stimulation experiments demonstrate that the device reproduces key synaptic plasticity behaviors, including postsynaptic current (PSC) and paired-pulse facilitation (PPF), with PSC amplitudes tunable by light intensity, pulse width, and frequency. Electrical stimulation tests further show that the device mimics nociceptive threshold responses, cumulative effects, and injury–recovery dynamics, enabling precise recognition of harmful stimuli. This study, for the first time, integrates light-controlled synaptic and electrically controlled nociceptive functionalities within a single HfS_2 device, offering a promising strategy for multimodal neuromorphic sensing systems.

Keywords:HfS_2, Self-Bent, Artificial Synapses, Nociceptors

Acknowledgement

I would like to express my deepest gratitude to my advisor, Dr. Lin Wang, for their unwavering guidance and support throughout the entirety of this project. From the initial conceptualization of my research to the final refinement of my work, Dr. Wang's expertise, patience, and insightful feedback have been instrumental in shaping my growth as a scholar.

Their willingness to take the time to discuss ideas, clarify complex concepts, and challenge me to think critically has not only elevated the quality of this project but also instilled in me a greater passion for my field. Beyond academic guidance, Dr. Wang has served as a mentor, offering valuable advice on navigating academic pursuits and encouraging me to embrace curiosity and resilience.

I feel incredibly fortunate to have had the opportunity to learn from such a dedicated and accomplished researcher. This work would not have been possible without their support, and I will carry the lessons I've learned under their guidance throughout my future endeavors. Thank you, Dr. Wang.

Commitments on Academic Honesty and Integrity

We hereby declare that we

1. are fully committed to the principle of honesty, integrity and fair play throughout the competition.
2. actually perform the research work ourselves and thus truly understand the content of the work.
3. observe the common standard of academic integrity adopted by most journals and degree theses.
4. have declared all the assistance and contribution we have received from any personnel, agency, institution, etc. for the research work.
5. undertake to avoid getting in touch with assessment panel members in a way that may lead to direct or indirect conflict of interest.
6. undertake to avoid any interaction with assessment panel members that would undermine the neutrality of the panel member and fairness of the assessment process.
7. observe the safety regulations of the laboratory(ies) where we conduct the experiment(s), if applicable.
8. observe all rules and regulations of the competition.
9. agree that the decision of YHSA is final in all matters related to the competition.

We understand and agree that failure to honour the above commitments may lead to disqualification from the competition and/or removal of reward, if applicable; that any unethical deeds, if found, will be disclosed to the school principal of team member(s) and relevant parties if deemed necessary; and that the decision of YHSA is final and no appeal will be accepted.

(Signatures of full team below)

X_____

Name of team member:

X_____

Name of supervising teacher:

CONTENTS

1 Introduction

In modern neuromorphic electronics, wearable healthcare devices, and artificial skin (e-skin), achieving high-sensitivity, low-power monitoring of nociceptors-particularly under synergistic photoelectronic stimulation-is of critical importance for brain-inspired systems[1, 2]. However, existing optical and electrical sensors are mostly discrete devices lacking a cooperative response mechanism, often requiring multiple components to realize multimodal perception. This not only increases system complexity, volume, and interface loss but also limits adaptability to flexible or curved substrates, thereby constraining their application in soft, contoured, or dynamic environments[3, 4]. Previous studies have explored the construction and challenges of flexible sensors from the perspectives of soft electronics, e-skin, and neural interfaces[5, 6]. Many flexible devices utilize metal microelectrodes embedded in polymers to achieve strain sensing and tactile detection[7, 8]. Concurrently, neuromorphic flexible sensing systems have emerged, integrating artificial synapses with sensing units to enable combined perception and processing; yet, these systems are often restricted to single-modality operations.

Hafnium disulfide (HfS2), a group IVB two-dimensional transition metal dichalcogenide [9], Hafnium disulfide (HfS2), a group IVB two-dimensional transition metal dichalcogenide[10-12]. Kanazawa et al.[13] experimentally characterized few-layer HfS2 field-effect transistors (FETs), reporting a carrier mobility of ~1800 cm2·V-1·s-1 and a bandgap of ~1.2 eV, highlighting its potential for low-power electronic applications. Subsequently, layered HfS2 has been employed in optoelectronic synaptic devices. Xiong et al.[14] designed HfS2-based optoelectronic synaptic devices capable of mimicking short-term and long-term memory, achieving ~88.5% accuracy in handwritten digit recognition. More recently, Wang et al.[15] constructed HfS2/VO2 heterojunctions demonstrating high responsivity (8.6×103 A/W) and detectivity (1.26×1014 Jones) under 405 nm laser illumination, successfully emulating the transition from short-term plasticity (STP) to

long-term plasticity (LTP) and even Pavlovian associative memory, illustrating thermally tunable synaptic behaviors. Moreover, strain engineering has been shown to significantly modulate carrier mobility in monolayer HfS2, with electronic mobility increasing by ~90% under tensile strain or decreasing by ~40% depending on the stress applied[16]. Kwon et al.[17] investigated synaptic plasticity in HfS2-based FETs, demonstrating paired-pulse facilitation under continuous light pulses at negative gate bias. Collectively, these studies highlight HfS2 as a material with high mobility, strain-tunable electronic properties, excellent optoelectronic response, and potential for phonon-thermal engineering. However, existing research mainly focuses on light-controlled synaptic behavior in single-material devices, and efforts to exploit HfS2's intrinsic structural features for "photo–electronic synergistic modulation" in a single-material system remain unexplored.

In this work, leveraging the superior optoelectronic performance and mechanical flexibility of HfS2, we exploit its spontaneous bending behavior to design and fabricate a flexible artificial synapse/nociceptor capable of synergistic photo-electronic perception within a single device. The device not only exhibits synaptic plasticity behaviors under optical and electrical stimulation-including short-term memory, long-term memory, and tunable synaptic weight modulation, but also enables multimodal perception and response through dual-stimulus synergy, thereby emulating complex neural signal transmission and nociceptive mechanisms. This strategy of integrating multiple perceptual functions within a single-material platform offers a new design paradigm for highly integrated, multifunctional intelligent sensing systems and lays a solid foundation for flexible e-skin, smart prosthetics, and next-generation human-machine interfaces.

2 Result and Discussion

2.1 materials synthesis and characterization

As shown in **Figure 1(a)**, the Raman spectra of the exfoliated HfS_2 flakes were recorded in the range of 100-800 cm^{-1}. Two prominent vibrational modes were observed at approximately 260 cm^{-1} and 338 cm^{-1}, corresponding to the in-plane E_g mode and the out-of-plane A_{1g} mode of HfS_2, respectively. In addition, a sharp peak near 520 cm^{-1} is attributed to the Si substrate, indicating that the flakes are sufficiently thin and well-adhered to the substrate. The Raman peak positions and relative intensities are consistent with previous reports, confirming the high crystallinity and phase purity of the HfS_2 flakes[18, 19]. As shown in **Figure 1(b)**, the optical bandgap of the HfS_2 films was further evaluated using room-temperature photoluminescence (PL) spectroscopy. Gaussian fitting of the PL spectra reveals a strong emission peak at approximately 1.13 eV, consistent with prior studies on few-layer HfS_2[20]. This result confirms the semiconducting nature of the material and highlights its potential for near-infrared optoelectronic applications. To investigate the device structure, atomic force microscopy (AFM) was employed to characterize the depth and morphology of the electrode channels (as shown in **Figure 1(c)**). The measured channel depth is approximately 300 nm, and the surface is smooth and uniform, providing a suitable trench structure for suspending HfS_2 flakes and enabling mechanical bending.

Figure 1(d) presents the suspended HfS_2 structures transferred onto pre-patterned electrode trenches. The left panel shows an optical microscopy image of a typical HfS_2 flake suspended across the electrode channel, while the right panel displays the AFM morphology and 3D height profile of the trench. It can be observed that the HfS_2 flake naturally bends over the 1 μm-wide trench, forming a suspended structure with a central deflection of approximately 83 nm. This confirms that the flake remains suspended above the trench bottom without collapse, and the naturally

curved geometry is critical for inducing local strain and enhancing carrier transport properties. **Figure 1(e)** shows the step height profile of the exfoliated HfS_2 flakes, indicating a thickness of approximately 12.5 nm, corresponding to 18-20 layers. This multilayer structure is suitable for simultaneously achieving mechanical flexibility and stable optoelectronic performance.

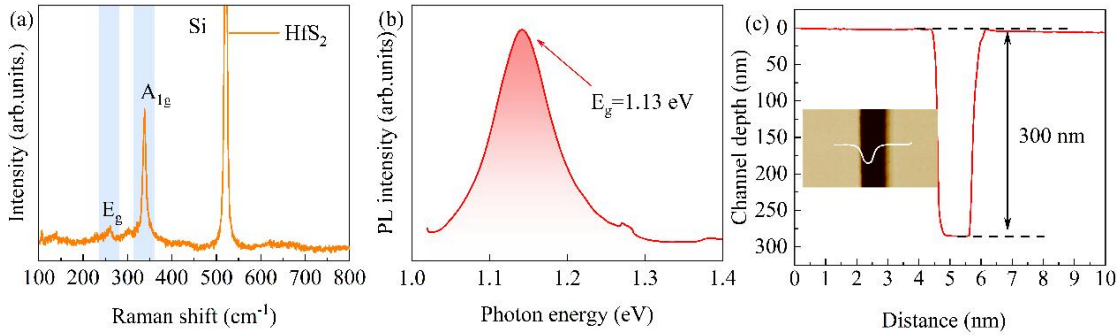

(a) Raman spectrum of an exfoliated HfS2 flake.

(b) Room-temperature photoluminescence (PL) spectrum of a 12.5 nm-thick HfS2 flake.

(c) AFM line-scan profile across the microfabricated trench, indicating a channel depth of ~300 nm with a uniform surface morphology.

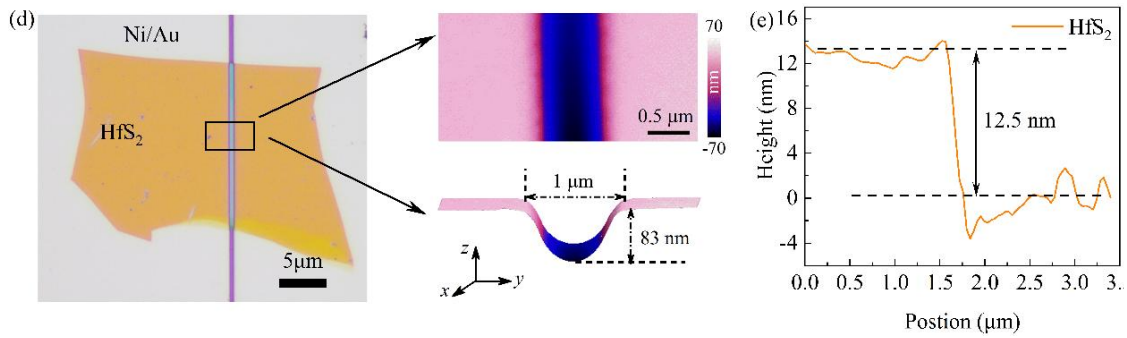

(d) Optical image (left) and corresponding AFM topography (right) of a suspended, self-bent HfS2 flake spanning a trench. The trench width is ~1 μm, and the central bending depth of the HfS2 flake is ~83 nm, as shown in the 3D reconstruction.

(e) AFM thickness profile of the HfS2 flake, indicating a film thickness of ~12.5 nm.

Figure 1 Structural and morphological characterization of HfS2 thin films and self-bent devices.

2.2 schematic diagram and structure characterization

To investigate the influence of mechanical deformation on the surface electronic properties of the suspended HfS_2 film, an in-situ Kelvin probe force microscopy

(KPFM) setup was designed and implemented, as illustrated in **Figure 2(a)**. The system integrates an externally controlled stimulus laser, excitation voltage, and a commercial AFM platform, enabling simultaneous acquisition of surface topography and local contact potential difference (CPD) distributions. This configuration is especially suitable for probing spatial variations in surface potential within suspended nanostructures. The KPFM technique allows visualization of the local work function variation by mapping the CPD, defined as:

$$V_{CPD} = (\Phi_{tip}-\Phi_{sample})/e \quad (1)$$

where Φ_{sample} and Φ_{tip} are the work functions of the sample and the probe tip, respectively, and e is the elementary charge. Since the tip's work function remains constant during scanning, a lower surface potential indicates a higher local work function of the HfS_2 flake.

As shown in **Figure 2(b)**, the KPFM potential map of the suspended device reveals a distinct contrast between the bent and flat regions of the HfS_2 flake. The central suspended region exhibits a significantly lower surface potential, implying a locally increased work function due to the strain-induced band modulation. This observation is further quantified in **Figure 2(c)**, where the extracted CPD profile clearly shows a potential well corresponding to the bent region of the flake. To elucidate the underlying mechanism, the band structure evolution under mechanical strain is schematically illustrated. As shown in **Figure 2(d)**, the flat HfS_2 flake exhibits a uniform energy band structure with evenly distributed carriers. In contrast, under non-uniform mechanical strain introduced by the suspended configuration, the conduction band minimum (CBM) and valence band maximum (VBM) of the HfS_2 shift upwards in the region experiencing tensile strain (positive curvature), as depicted in **Figure 2(e)**. This band bending results in a type-II intramolecular heterojunction centered at the midpoint of the suspended trench, where carrier redistribution and local polarization effects can occur. The formation of this built-in electric field is

expected to enhance carrier separation and contribute to the device's optoelectronic functionality, particularly in synaptic and nociceptive emulation.

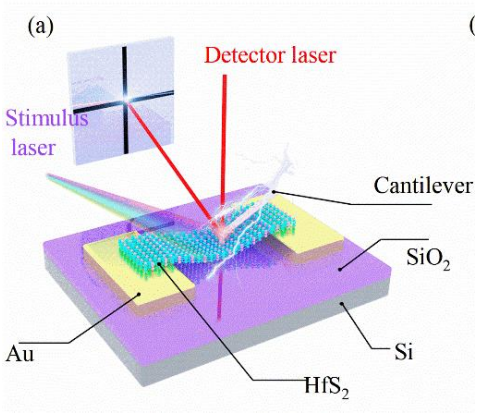

(a) Schematic of the in-situ KPFM measurement setup for the suspended HfS2 device.

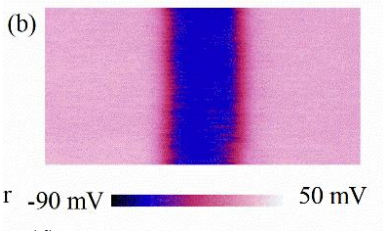

(b) KPFM surface potential map showing lower potential in the bent region.

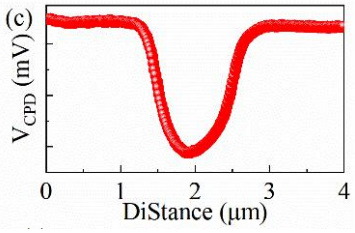

(c) Extracted CPD profile along the trench direction, revealing a potential dip at the center.

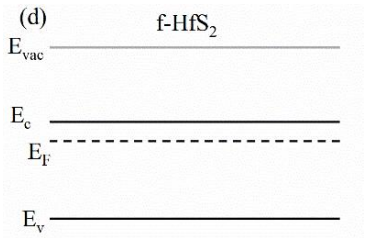

(d) Schematic energy band diagram of flat HfS2.

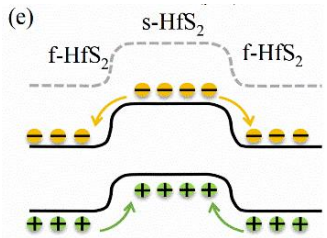

(e) Strain-induced band modulation and formation of type-II intramolecular heterojunction in the suspended HfS2 flake.

Figure 2 In-situ KPFM characterization of suspended HfS_2 flake.

2.3 optical characterization

In biological neural systems, adjacent neurons are interconnected via synapses, where signals are transmitted from the presynaptic neuron to the postsynaptic neuron through neurotransmitters, generating postsynaptic currents (PSC). PSCs constitute the core mechanism for information transmission, processing, and storage in neural networks and are fundamental to synaptic function. **Figure 3(a)** schematically

illustrates biological neurons and the synaptic transmission process. In this work, optical pulses are regarded as presynaptic signals, while the device drain-source current (I_{ds}) serves as the postsynaptic response.

As shown in **Figure 3(b)**, under 405 nm ultraviolet pulse illumination (power density 39.01 mW/cm^2, pulse width 5 s), the heterojunction transistor exhibits a typical PSC response: the PSC rapidly rises to approximately 0.35 μA during light exposure, and upon removal of the optical stimulus, PSC gradually returns to its initial value due to charge trapping effects at defect states. To further evaluate the optoelectronic performance, I-V measurements of the bent HfS_2 device were conducted, demonstrating clear rectifying behavior.

To extract the current rise dynamics, the I-t curve was fitted using a double-exponential model (as shown in **Figure 3(c)**):

$$I=I_0+Ae^{-\frac{t}{\tau_1}}+Be^{-\frac{t}{\tau_2}} \quad (2)$$

where I_0 represents the steady-state photocurrent, A and B are fitting constants, and τ_1 and τ_2 correspond to the relaxation times of the fast and slow response components during the rising stage, respectively. Fitting results yield τ_1=7.26 ms and τ_2=189 ms for the bent HfS_2 device, indicating rapid initial response followed by a slower relaxation process.

To investigate the pulse intensity-dependent synaptic plasticity, single optical pulses with varying power densities (0.012~39.01 mW/cm^2) were applied under fixed pulse width (500 ms) and V_{ds}=3V, and the temporal evolution of PSC was recorded (as shown in **Figure 3(d)**). The results show that PSC amplitude increases with light intensity, demonstrating that the synaptic device effectively mimics the enhancement of synaptic weight observed in biological learning processes. Analogous to a learning process, the PSC rise corresponds to enhanced synaptic responsiveness upon stimulus, while the current decay simulates the natural forgetting of memory over time, resembling the trend described by the Ebbinghaus forgetting curve.

The relationship between optical pulse intensity and learning efficacy can be quantified using the single-pulse index (ΔPSC/PSC):

$$\frac{\Delta PSC}{PSC} = \frac{A\text{-}A_0}{A} \times 100\% \quad (3)$$

where A and A_0 represent the PSC amplitude after and before laser illumination, respectively. As shown in **Figure 3(d)**, the single-pulse index increases with power density and saturates above 8.40 mW/cm^2, indicating that at a fixed pulse width of 500 ms, the device's "learning capability" reaches saturation at a power density of 8.40 mW/cm^2.

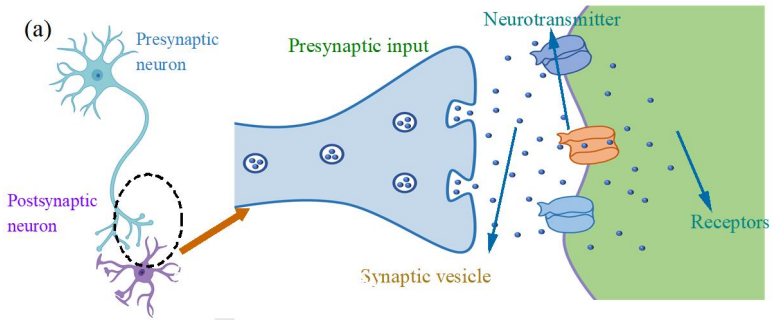

(a) Schematic illustration of a single biological synapse structure.

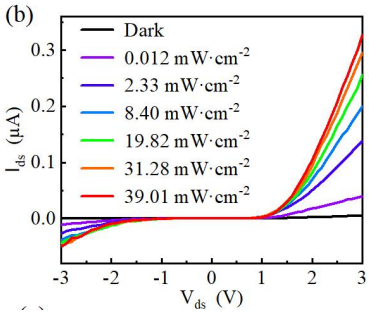

(b) Current–voltage (Ids-Vds) characteristics of the HfS_2 device under various laser power densities at room temperature (λ= 405 nm).

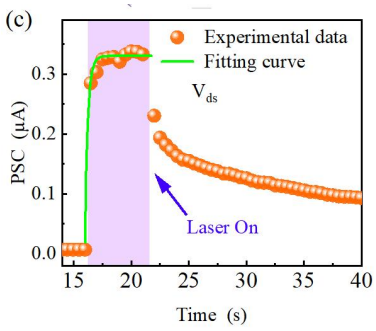

(c) Post-synaptic current (PSC) response under a single 405 nm laser pulse.

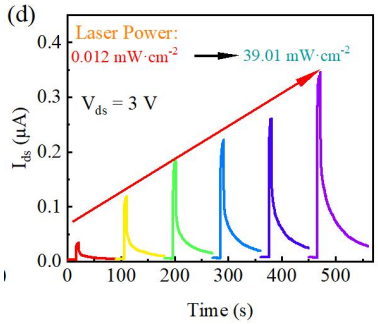

(d) Temporal evolution of PSC triggered by single light pulses with different power densities at a fixed bias of Vds=3V.

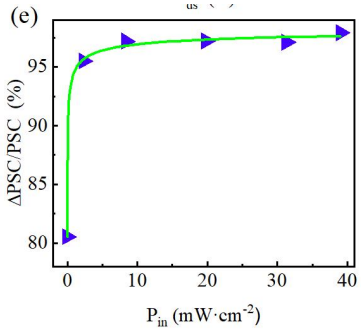

(e) Relative synaptic weight change (ΔPSC/PSC) as a function of light power density.

Figure 3

In the field of artificial synapses and synaptic plasticity, semiconductor materials and devices capable of emulating biological synaptic behavior have attracted significant attention. Synaptic plasticity is a core mechanism underlying learning and memory in neural networks, typically regulated by the duration of stimulus signals in biological systems. Inspired by this, we employed the bent HfS_2 device system to investigate the effect of optical pulse width on artificial synaptic performance.

To explore the evolution of postsynaptic current (PSC) under different pulse widths, single-pulse optical stimulations with a fixed laser power density of 39.01 $mW \cdot cm^{-2}$ and pulse widths ranging from 100 to 900 ms were applied. As shown in **Figure 4(a)**, the PSC peak significantly increases with pulse width, consistent with the plasticity characteristics associated with stimulus duration. This indicates that extending the ultraviolet pulse duration generates more photocarriers, effectively enhancing PSC amplitude and memory retention.

The PSC decay behavior was evaluated using the Kohlrausch stretched-exponential function [21]:

$$PSC=A_0+A_1\times\exp\left(-\left(\frac{t}{\tau}\right)^{\beta}\right) \quad (4)$$

where t is time, β is the stretching exponent, and τ represents the carrier retention time in the device. As shown in **Figure 4(b)**, under a laser power density of 39.01 mW/cm^2 and pulse width of 500 ms, the extracted stretching exponent is 0.122, and the retention time τ is approximately 225.2 ms, indicating a characteristic carrier migration timescale of 225.2 ms.

Short-term plasticity (STP) and long-term plasticity (LTP) are two key mechanisms for neural information processing and memory formation[22, 23]. STP is mainly associated with transient information recognition, whereas LTP corresponds to the formation of persistent memory. In synaptic transistors, the transition from STP to LTP can be achieved by increasing optical power density, pulse width, pulse number, or stimulation frequency. To further validate the device's plasticity modulation capability, we examined responses under multiple pulse stimulations (**Figure 4(c)**). The results show that increasing optical power density or pulse number significantly enhances PSC amplitude and prolongs decay time, as stronger illumination generates more photocarriers and extends their recombination lifetime, thereby exhibiting pronounced LTP characteristics.

In addition to pulse duration and intensity, pulse frequency is another critical factor influencing the STP-to-LTP transition. **Figure 4(d)** presents PSC responses under a fixed pulse width of 500 ms, power density of 39.01 $mW \cdot cm^{-2}$, and frequency range of 0.2~1.25 Hz. With increasing frequency, both PSC amplitude and retention time increase markedly. This effect is attributed to the shortened intervals between pulses at high frequency, which suppresses carrier recombination and enhances the cumulative photonic response. Under a fixed pulse number of 10, PSC rises from 0.3 μA (0.2 Hz) to 0.45 μA (1.25 Hz), exhibiting a clear frequency-dependent gain (Gain = A_0/A_1). Such frequency-dependent behavior resembles a high-pass filter, effectively highlighting high-frequency components of input signals, which is significant for neuromorphic computing and image processing[24, 25].

Paired-pulse facilitation (PPF) is an important manifestation of STP, reflecting cumulative effects in the presynaptic membrane under consecutive stimuli. PPF is defined as[26]:

$$PPF=\frac{A_2}{A_1}\times 100\% \tag{5}$$

where A_1 and A_2 are the PSC peak currents triggered by the first and second pulses, respectively, as shown in **Figure 4(e)**. Under 405 nm illumination, 500 ms pulse width, and 39.01 $mW \cdot cm^{-2}$ power density, PPF was measured at different inter-pulse intervals (Δt) (**Figure 4(f)**). With increasing Δt, PPF decreases from a maximum of ~118% (Δt=0.8 s) to ~102%, consistent with biological synaptic behavior [27, 28]:

$$PPF=1+C_1\times e^{(-\frac{\Delta t}{\tau_1})}+C_2\times e^{(-\frac{\Delta t}{\tau_2})} \tag{6}$$

where C1 and C2 represent the fast and slow relaxation amplitudes, and τ_1 and τ_2 correspond to characteristic times for rapid carrier transport and slower ion diffusion (or defect-state interactions), respectively. Fitting results yield τ_1=82 ms and τ_2=1.38 s, closely matching typical biological synaptic measurements, further confirming the device's effectiveness in emulating short-term synaptic plasticity[29].

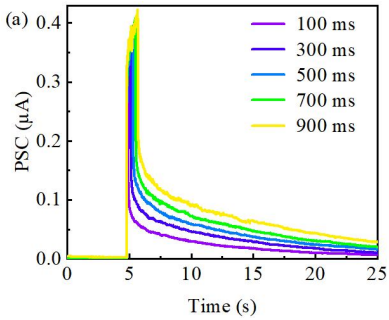

(a) PSC response curves as a function of optical pulse width (405 nm, 39.01 mW·cm-2);

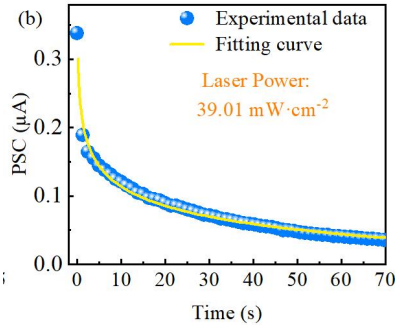

(b) representative PSC decay curve with Kohlrausch stretched-exponential fitting;

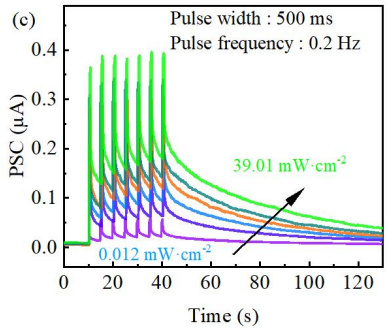

(c) multi-pulse PSC responses under varying pulse numbers and power densities;

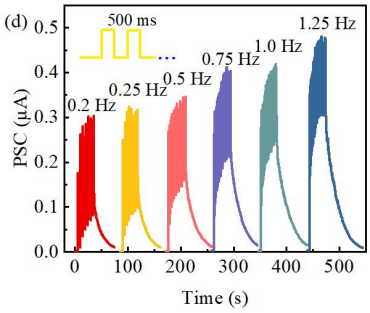

(d) PSC variations under different pulse frequencies (fixed pulse number = 10, width = 500 ms, power = 39.01 mW·cm-2) and frequency-dependent gain;

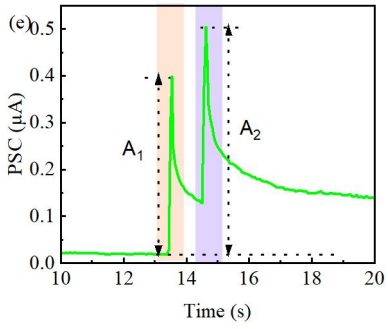

(e) PPF effect triggered by paired 500 ms pulses;

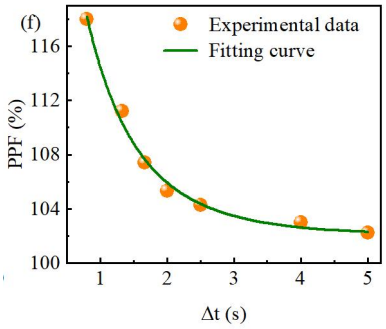

(f) PPF curves at different inter-pulse intervals with double-exponential fitting, showing fast and slow relaxation consistent with biological synapses.

Figure 4

2.4 electrical characterization

Figure 5(a) schematically illustrates the working mechanism of the human nociceptor system. Nociceptors are widely distributed throughout the body and can detect harmful external stimuli, such as temperature, pressure, or chemical agents.

Upon sensing a noxious stimulus, nociceptors generate action potentials that propagate along nerve fibers to the central nervous system (spinal cord and brain), where the signals are processed to elicit pain perception.

To investigate the basic behavior of the bent HfS_2 device in artificial nociception, electrical pulses of varying amplitude and duration were applied to simulate external stimuli. A 5-minute interval was maintained between consecutive experiments to avoid interference and ensure full recovery of the device to its high-resistance state (HRS). As shown in **Figure 5(b)**, when the input pulse amplitude reaches 7 V, the device output current attains 0.25 μA, defined as the noxious current (I_{nox}), corresponding to the device's nociceptive threshold. The results indicate that for pulse amplitudes below 7 V, the device remains in the HRS, and the output current is below I_{nox}. Once the amplitude reaches or exceeds 7 V, the output current rapidly surpasses I_{nox}, activating the nociceptive response. Higher stimulus amplitudes produce larger output currents, reflecting the device's sensitivity to stimulus intensity.

Figure 5(c) shows the device response under a fixed pulse amplitude of 7 V with varying pulse durations (0.1-8 s). When the pulse duration is less than 1.5 s, the output current remains below I_{nox}, indicating an inactive state. When the pulse duration reaches or exceeds 1.5 s, the output current exceeds I_{nox}, demonstrating that longer pulses can induce cumulative effects and enhance nociceptive responses, consistent with biological nociceptors' ability to amplify perception under sustained stimulation.

To further elucidate the relationship between stimulus intensity and device response, pulse amplitudes were varied from 0 to 12 V in 1 V increments, with pulse durations ranging from 0.1 to 3 s. **Figure 5(d)** presents a contour map of the output current as a function of pulse amplitude and duration, where the green-shaded region represents I_{nox} (0.25 μA), and the dashed line indicates the threshold boundary. The region with output current > I_{nox} corresponds to device activation, whereas output current < I_{nox} indicates the HRS. The results show that at low voltages (< 6 V),

extending the pulse duration has limited effect on output current, while at higher voltages, even short pulses can trigger activation.

Figure 5(g) depicts the output responses under multiple pulses of varying amplitudes (pulse width 0.1 s, interval 0.1 s). At 6 V, the output current remains below I_{nox} despite repeated pulses, whereas at 7 V and 9 V, the current exceeds I_{nox} at the 28th and 12th pulses, respectively, indicating that higher pulse amplitudes reduce the required cumulative stimulation to trigger activation.

In biological systems, damaged nociceptors often exhibit two distinct features: allodynia (pain evoked by normally innocuous stimuli) and hyperalgesia (exaggerated pain response to noxious stimuli). **Figure 5(e)** simulates the damaged state: an initial 10 V pulse induces "injury," followed by pulses of 6~9 V. The damaged device is activated at lower voltages (allodynia), and at higher voltages, the response speed and intensity are significantly enhanced (hyperalgesia).

Furthermore, biological nociceptors possess self-repair capabilities to restore normal function. To verify the repairability of the bent HfS_2 device, a 10 V pulse was first applied to simulate damage, and then 7 V pulses were applied after varying recovery intervals (3 s, 5 s, 10 s, 20 s) in **Figure 5(f)**. The results show that the output current gradually returns to normal as the recovery time increases, and at 20 s, the device fully recovers to the HRS, indicating complete repair of the simulated damage.

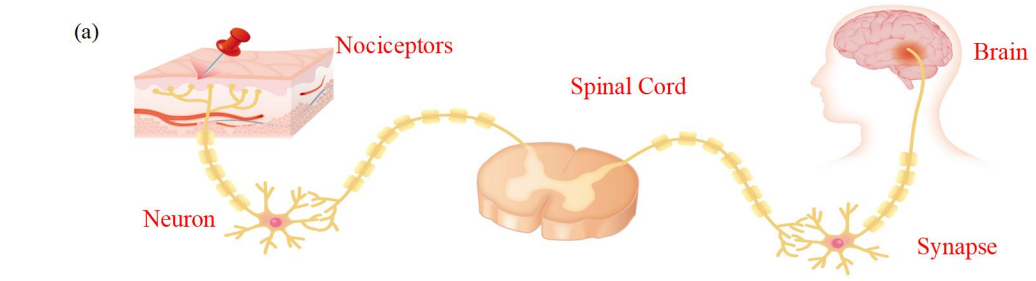

(a) Schematic of the human nociceptor system;

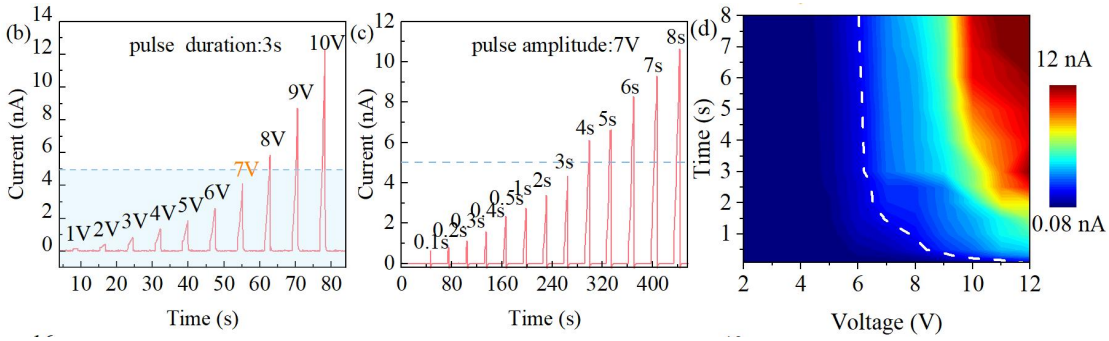

(b) device current responses under different pulse amplitudes;

(c) current responses at 7 V for varying pulse durations;

(d) contour map of output current as a function of input voltage amplitude (0~12 V) and pulse duration (0.1~3 s);

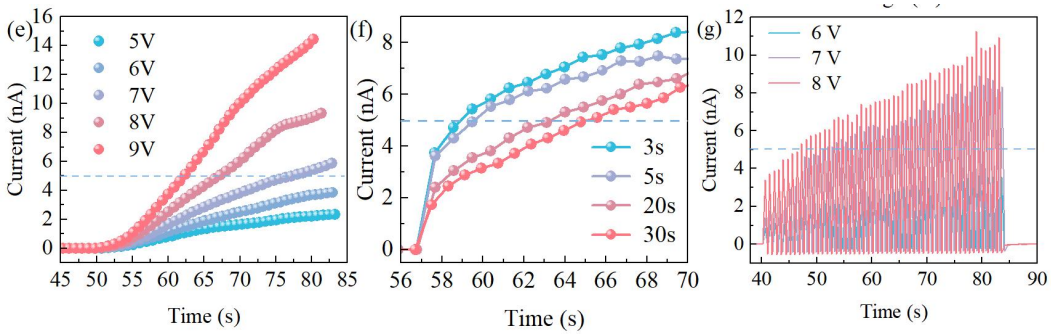

(e) responses under 5~9 V pulses after simulated damage with a 10 V pulse, showing allodynia and hyperalgesia;

(f) current responses after recovery intervals of 3 s, 5 s, 10 s, 20 s, and 30 s following 10 V induced damage, demonstrating repairability;

(g) output responses under multiple pulses with varying amplitudes (blue dashed line indicates I_{nox} threshold).

Figure 5

3 Conclusion and discussion

In this work, we successfully constructed a flexible device that integrates both optically controlled synaptic functions and electrically controlled nociceptive responses by exploiting the spontaneous bending characteristics of two-dimensional HfS_2. The bent HfS_2 forms a type-II intramolecular heterojunction due to non-uniform

strain, which enhances carrier separation via the built-in electric field and provides a physical basis for light–electric cooperative responses. Characterization by Raman spectroscopy, photoluminescence (PL), and atomic force microscopy (AFM) confirms the high crystallinity and appropriate thickness (~12.5 nm) of the material, ensuring a balance between mechanical flexibility and optoelectronic performance. Functionally, under optical stimulation, the device reliably emulates post-synaptic currents (PSC), short-term and long-term plasticity (STP/LTP), and paired-pulse facilitation (PPF), with response characteristics tunable by light intensity, pulse width, and frequency, consistent with learning and memory behavior observed in biological synapses. Under electrical stimulation, the device accurately reproduces nociceptive threshold responses (7 V), cumulative effects (pulse duration ≥1.5 s), and injury–repair behaviors, effectively mimicking biological features such as allodynia and hyperalgesia.

This work demonstrates that by leveraging the spontaneous bending of HfS_2, light–electric cooperative perception can be realized in a single device, overcoming the functional limitations of traditional discrete devices. The integration of synaptic and nociceptive functionalities without the need for additional heterojunctions simplifies the fabrication process and provides a novel paradigm for high-integration neuromorphic systems.

4 Experimental Process

High-quality HfS_2 crystals (purchased from Six Carbon Technology, Shenzhen) were mechanically exfoliated using adhesive tape to obtain thin flakes. These exfoliated flakes were first transferred onto a PDMS (polydimethylsiloxane) film (Shanghai Angwei Technology Co., Ltd.) for temporary handling and observation. Optically thin flakes with suitable thickness and uniform morphology were then identified under an optical microscope and subsequently transferred onto a Si/SiO_2 substrate (Metatest, model: E1-T) to fabricate the flexible HfS_2-based devices. The thickness and surface morphology of the transferred HfS_2 flakes were characterized

using atomic force microscopy (AFM, Dimension Icon, Bruker) and optical microscopy. To further analyze the surface electrical characteristics, Kelvin probe force microscopy (KPFM, also Dimension Icon, Bruker) measurements were performed in a dark environment to eliminate photo-induced artifacts and ensure reliable surface potential mapping. Raman spectroscopy was conducted to confirm the crystal quality and vibrational characteristics of the HfS_2 flakes. The measurements were carried out using a confocal Raman microscope (LabRAM HR Evolution, HORIBA) with a 532 nm laser excitation source. All spectra were acquired at room temperature under ambient conditions unless otherwise specified. Electrical and optoelectronic properties of the devices were investigated using a Keithley 4200-SCS semiconductor parameter analyzer under high vacuum and at room temperature. For photoresponse measurements, a 405 nm laser diode (Thorlabs, Inc.) was employed to ensure wavelength specificity and reduce ambient light interference. During illumination, the light intensity, pulse duration, and repetition frequency were precisely controlled through a laser diode driver and integrated temperature controller, enabling accurate simulation of optical stimuli under various dynamic conditions.

Reference

[1] Y. J. Fan, X. Li, S. Y. Kuang, Y. Kuang, L. Zhang, Y. H. Chen, L. Liu, K. Zhang, S. W. Ma, F. Liang, T. Wu, Z. L. Wang, G. Zhu. Highly Robust, Transparent, and Breathable Epidermal Electrode [J]. *Acs Nano*, 2018, 12(9): 9326-9332.

[2] P. Rwei, J. W. Shiu, M. Senel, A. Hajiaghajani, C. Y. Qian, C. W. Chen, P. Tseng, M. Khine. A Waterborne, Flexible, and Highly Conductive Silver Ink for Ultra-Rapid Fabrication of Epidermal Electronics [J]. *Sensors-Basel*, 2025, 25(7).

[3] I. M. Graz, D. P. J. Cotton, A. Robinson, S. P. Lacour. Silicone substrate with strain relief for stretchable thin-film transistors [J]. *Applied Physics Letters*, 2011, 98(12).

[4] A. C. Bunea, V. Dediu, E. A. Laszlo, F. Pistritu, M. Carp, F. S. Iliescu, O. N. Ionescu, C. Iliescu. E-Skin: The Dawn of a New Era of On-Body Monitoring Systems [J]. *Micromachines-Basel*, 2021, 12(9).

[5] S. Y. Wu, Z. Sha, L. Wu, H. P. Phan, S. He, J. B. Tang, J. T. Xu, D. W. Chu, C. H. Wang, S. H. Peng. Recent advances in multimodal skin-like wearable sensors [J]. *Appl Phys Rev*, 2024, 11(4).

[6] X. D. Sun, X. Guo, J. S. Gao, J. Wu, F. C. Huang, J. H. Zhang, F. H. Huang, X. Lu, Y. Shi, L. J. Pan. E-Skin and Its Advanced Applications in Ubiquitous Health Monitoring [J]. *Biomedicines*, 2024, 12(10).

[7] Q. F. Lu, Y. C. Zhao, L. Huang, J. B. An, Y. F. Zheng, E. H. Yap. Low-Dimensional-Materials-Based Flexible Artificial Synapse: Materials, Devices, and Systems [J]. *Nanomaterials-Basel*, 2023, 13(3).

[8] Y. Wang, Y. Y. Zhu, Y. Y. Li, Y. Q. Zhang, D. R. Yang, X. D. Pi. Dual-Modal Optoelectronic Synaptic Devices with Versatile Synaptic Plasticity [J]. *Advanced Functional Materials*, 2022, 32(1).

[9] M. Son, H. Jang, D. B. Seo, J. H. Lee, J. Kim, M. Kim, S. Kang, S. Yim, W. Song, J. W. Yoo, H. Y. Kim, S. S. Lee, K. S. An. High-Performance Infrared Photodetectors Driven by Interlayer Exciton in a Van Der Waals Epitaxy Grown HfS_2/MoS_2 Vertical Heterojunction [J]. *Advanced Functional Materials*, 2024, 34(7).

[10] K. Xu, Z. X. Wang, F. Wang, Y. Huang, F. M. Wang, L. Yin, C. Jiang, J. He. Ultrasensitive Phototransistors Based on Few-Layered HfS_2 [J]. *Advanced Materials*, 2015, 27(47): 7881-7887.

[11] L. Fu, F. Wang, B. Wu, N. Wu, W. Huang, H. L. Wang, C. H. Jin, L. Zhuang, J. He, L. Fu, Y. Q. Liu. Van der Waals Epitaxial Growth of Atomic Layered HfS_2 Crystals for Ultrasensitive Near-Infrared Phototransistors [J]. *Advanced Materials*, 2017, 29(32).

[12] B. Wang, X. K. Luo, J. L. Chang, X. R. Chen, H. K. Yuan, H. Chen. Efficient charge separation and visible-light response in bilayer HfS_2-based van der Waals heterostructures [J]. *Rsc Adv*, 2018, 8(34): 18889-18895.

[13] T. Kanazawa, T. Amemiya, A. Ishikawa, V. Upadhyaya, K. Tsuruta, T. Tanaka, Y. Miyamoto. Few-layer HfS_2 transistors [J]. *Sci Rep-Uk*, 2016, 6.

[14] H. Xiong, L. P. Xu, C. F. Gao, Q. Zhang, M. H. Deng, Q. F. Wang, J. Z. Zhang, D. Fuchs, W. W. Li, A. Y. Cui, L. Y. Shang, K. Jiang, Z. G. Hu, J. H. Chu. Optically Modulated HfS_2-Based Synapses for Artificial Vision Systems [J]. *Acs Applied Materials & Interfaces*, 2021, 13(42): 50132-50140.

[15] L. Wang, L. Wang, X. Y. Ye, X. H. Xu, L. Y. Shang, Y. W. Li, J. Z. Zhang, L. Q. Zhu, Z. G. Hu. Thermally modulated photoelectronic synaptic behavior in HfS_2/VO_2 heterostructure [J]. *Rare Metals*, 2024, 43(8): 3798-3809.

[16] Y. F. Chung, S. T. Chang. Enhanced Carrier Transport Performance of Monolayer Hafnium Disulphide by Strain Engineering [J]. *Nanomaterials-Basel*, 2024, 14(17).

[17] M. J. Kwon, N. V. Binh, S. Y. Cho, S. B. Shim, S. H. Ryu, Y. J. Jung, W. H. Nam, J. Y. Cho, J. H. Park. Optoelectronic Synapse Behaviors of HfS_2 Grown via Molten Salt Flux Method [J]. *Electron Mater Lett*, 2024, 20(5): 559-570.

[18] Q. F. Wang, R. Q. Jiang, Z. T. Gao, M. H. Deng, J. H. Chen, L. Q. Zhu, L. Y. Shang, Y. W. Li, D. Fuchs, J. Z. Zhang, Z. G. Hu. A HfS_2-based photoelectronic synaptic transistor with tunable synaptic plasticity for emotional memory [J]. *Applied Surface Science*, 2023, 613.

[19] B. J. Zheng, Y. F. Chen, Z. G. Wang, F. Qi, Z. S. Huang, X. Hao, P. J. Li, W. L. Zhang, Y. R. Li. Vertically oriented few-layered HfS_2 nanosheets: growth mechanism and optical properties [J]. *2d Materials*, 2016, 3(3).

[20] C. Y. Yan, L. Gan, X. Zhou, J. Guo, W. J. Huang, J. W. Huang, B. Jin, J. Xiong, T. Y. Zhai, Y. R. Li. Space-Confined Chemical Vapor Deposition Synthesis of Ultrathin HfS_2 Flakes for Optoelectronic Application [J]. *Advanced Functional Materials*, 2017, 27(39).

[21] C. Han, X. W. Han, J. Y. Han, M. Y. He, S. L. Peng, C. Y. Zhang, X. C. Liu, J. Gou, J. Wang. Light-Stimulated Synaptic Transistor with High PPF Feature for Artificial Visual Perception System Application [J]. *Advanced Functional Materials*, 2022, 32(22).

[22] Y. Ren, L. Hu, J. Y. Mao, J. Yuan, Y. J. Zeng, S. C. Ruan, J. Q. Yang, L. Zhou, Y. Zhou, S. T. Han. Phosphorene nano-heterostructure based memristors with broadband response synaptic plasticity [J]. *J Mater Chem C*, 2018, 6(35).

[23] [23] N. W. Oesch, J. S. Diamond. Synaptic inhibition tunes contrast computation in the retina [J]. *Visual Neurosci*, 2019, 36.

[24] Y. H. Zhou, J. Li, Y. H. Yang, Q. Chen, J. H. Zhang. Artificial Synapse Emulated through Fully Aqueous Solution Processed Low-Voltage In_2O_3 Thin-Film Transistor with Gd_2O_3 Solid Electrolyte [J]. *Acs Applied Materials & Interfaces*, 2020, 12(1): 980-988.

[25] J. Jiang, W. N. Hu, D. D. Xie, J. L. Yang, J. He, Y. L. Gao, Q. Wan. 2D electric-double-layer phototransistor for photoelectronic and spatiotemporal hybrid neuromorphic integration [J]. *Nanoscale*, 2019, 11(3): 1360-1369.

[26] J. Murakami, R. Okada, Y. Fujito, M. Sakakibara, K. Lukowiak, E. Ito. Paired pulse ratio analysis of insulin-induced synaptic plasticity in the snail brain [J]. *J Exp Biol*, 2013, 216(10): 1771-1773.

[27] Y. Wang, L. Yin, W. Huang, Y. Y. Li, S. J. Huang, Y. Y. Zhu, D. R. Yang, X. D. Pi. Optoelectronic Synaptic Devices for Neuromorphic Computing [J]. *Adv Intell Syst-Ger*, 2021, 3(1).

[28] D. Kim, W. K. Min, H. T. Kim, J. Chung, M. S. Kim, H. J. Kim. Realization of Enhanced Long-Term Visual Memory for Indium-Gallium-Zinc Oxide-Based Optical Synaptic Transistor [J]. *Adv Opt Mater*, 2022, 10(15).

[29] X. L. Chen, J. Y. Pan, J. J. Fu, X. Zhu, C. Zhang, L. Zhou, Y. Wang, Z. Y. Lv, Y. Zhou, S. T. Han. Polyoxometalates-Modulated Reduced Graphene Oxide Flash Memory with Ambipolar Trapping as Bidirectional Artificial Synapse [J]. *Adv Electron Mater*, 2018, 4(12).